Chemical Science

ROYAL SOCIETY OF CHEMISTRY

EDGE ARTICLE

View Article Online
View Journal | View Issue

Cite this: *Chem. Sci.*, 2025, **16**, 21962

All publication charges for this article have been paid for by the Royal Society of Chemistry

Received 14th July 2025
Accepted 1st October 2025

DOI: 10.1039/d5sc05222j

rsc.li/chemical-science

A novel near-infrared fluorescent hERG potassium channel probe for glioblastoma therapy and imaging

Zhenzhen Liu, †*[a] Li Liu,†[a] Tongtong Ban,†[a] Xin Wang, [a] Ruihao Li,[a] Xiao Zhang,[a] Yuanwen Wang,[a] Xiaojuan Li,[a] Wei Zhang,[a] Ping Li *[ab] and Bo Tang [ac]

Glioblastoma multiforme (GBM) is the most common and malignant type of primary brain tumor, and its therapy remains challenging. The hERG potassium channel represents a promising target for GBM therapy and imaging. However, there are currently few efficient hERG channel inhibitors with low toxicity for cancer therapy. In this work, a novel near-infrared fluorescent probe A8 with high binding affinity for the hERG channel was developed, and then it was encapsulated into an ApoE peptide-modified liposome to improve its transport across the blood–brain barrier and tumor targeting. The obtained liposome, ApoE-Lipo@A8, can significantly suppress the growth of orthotopic glioblastoma xenografts with reduced cardiac toxicity. Additionally, our studies unveil a novel molecular mechanism underlying the antitumor effect of hERG channel inhibition, including suppression of the CDK2-pRB-E2F axis and induction of ER-stress-dependent apoptosis and autophagy. Additionally, A8 is characterized by an aggregation-caused fluorescence quenching switch, and it can be used to light up the hERG channel and, further, for GBM imaging *in vivo*. Together, this study systematically explores the therapeutic and imaging potential of the hERG channel for glioblastomas using the probe A8, which would promote the development of the hERG channel as a therapeutic and imaging target for cancer.

Introduction

Glioblastoma multiforme (GBM) is the most malignant and aggressive primary tumor in the central nervous system.[1,2] The standard clinical treatment for GBM patients is surgical resection of tumors followed by radiotherapy and chemotherapy. Nevertheless, due to its extensive infiltration properties, it is difficult to completely remove the tumor tissues without affecting normal brain function. As a result, tumor recurrence is common after surgery. Alkylating agents that can easily cross the blood–brain barrier (*e.g.* temozolomide, carmustine and lomustine) are first-line chemotherapy drugs used clinically. However, they are prone to inducing resistance after a period of use, leading to a significant decrease in their therapeutic efficacy.[3,4] Therefore, the current clinical treatment effects for GBM are still not satisfactory, and the prognosis of patients is very poor, with a median survival of only 15–16 months and a 5 year survival rate of 5%. To improve the clinical treatment outcomes for GBM, bevacizumab, trametinib and some other targeted drugs and immunotherapy (vaccine therapy, immune checkpoint inhibitors, chimeric antigen receptor T (CAR-T) cell therapy, oncolytic virus therapy, and vaccine therapy) have also been investigated for the treatment of GBM.[5–9] Unfortunately, the survival rates of patients still have not substantially improved. Therefore, novel therapeutic strategies for GBM remain urgently needed to improve the prognosis of glioblastoma patients.

Ion channels are crucial membrane proteins that possess a gated pore structure, allowing various water-soluble ions (such as Na^+, Cl^-, K^+, Ca^{2+}, H^+, *etc.*) and substances to pass through, and they are targeted by 18% of FDA-approved drugs, ranking second only to G protein-coupled receptors (GPCRs, 33%). Of these, the hERG potassium channel is a type of voltage-gated potassium channel that contributes to the rapid delayed rectifier potassium current (I_{Kr}). It plays an important role in the repolarization phase of the cardiac action potential.[10] Interestingly, extensive research has shown that hERG potassium channels are overexpressed in various types of cancer tissues, such as leukemia, gastric cancer, colon cancer and breast cancer.[11–15] Subsequent studies revealed that the hERG channel extensively participates in tumor cell proliferation, apoptosis, metastasis, invasion, neovascularization and cell volume regulation, thereby promoting tumor initiation and progression.[16]

[a]*College of Chemistry, Chemical Engineering and Materials Science, Key Laboratory of Molecular and Nano Probes, Ministry of Education, Collaborative Innovation Center of Functionalized Probes for Chemical Imaging in Universities of Shandong, Institutes of Biomedical Sciences, Shandong Normal University, Jinan, 250014, China. E-mail: zzliu@sdnu.edu.cn; lip@sdnu.edu.cn*

[b]*College of Chemistry and Chemical Engineering, Northwest Normal University, Lanzhou, 730070, China*

[c]*Laoshan Laboratory, Qingdao, 266237, People's Republic of China*

† Co-first authors and they contributed equally to this work

Similarly, for GBM tumors, high levels of hERG potassium channels have been detected in both *in vitro* cultured and *in situ* tumor cells, while there was no or lower expression in normal astrocytes and low-grade glioma cells.[15,17] In particular, Masi *et al.* found that hERG potassium channels can promote the secretion of vascular endothelial growth factor (VEGF) in GBM cell lines, which is crucial for tumor angiogenesis.[15] The John S. Kuo group constructed an *in situ* GBM mouse model using tumor cells from clinical GBM patients and studied the impact of hERG channels on tumor cell proliferation at the *in vivo* level.[18] The results showed that higher levels of hERG potassium channels were associated with a faster tumor cell proliferation rate. Furthermore, they analyzed a series of tumor tissue samples from clinical GBM patients and found that GBM patients with high expression levels of hERG potassium channels had shorter survival periods compared to those with low expression levels. These studies for the first time revealed the clinical significance of the hERG potassium channel for GBM treatment. In addition, we conducted survival analysis based on TCGA (the Cancer Genome Atlas) and CGGA (Chinese Glioma Genome Atlas) databases (SI Fig. S10). Consistently, it was found that patients with high expression levels of hERG potassium channels had significantly shorter survival times. Therefore, the hERG potassium channel is a promising therapeutic target for GBM therapy, and it can also serve as a biomarker for predicting patient survival. However, there are few efficient hERG channel inhibitors with low toxicity for cancer therapy,[5,19] which has impeded the application of the hERG channel as a cancer therapeutic target. Meanwhile, detailed molecular mechanisms underlying the contribution of the hERG channel to tumor initiation and development or the antitumor effects of hERG blockades have also not been well elucidated.

Optical imaging, including fluorescence imaging, bioluminescence imaging, and optical coherence tomography imaging, has the characteristics of high resolution, high contrast and convenience. It has been broadly applied in biological molecule labeling, intraoperative navigation and disease diagnosis. At present, there are only a few fluorescent probes used for clinical GBM imaging, including 5-ALA, ICG and fluorescein.[20] However, 5-ALA needs to be metabolized into protoporphyrin IX (PpIX) before it can be used for GBM imaging, so some patients may show no response. Additionally, the excitation wavelength of PpIX is 405 nm, which results in high background interference. ICG and fluorescein take advantage of the compromised blood–brain barrier at the tumor site to passively target GBM tumors, and they mainly accumulate in the extracellular region, so their specificity for GBM imaging is poor. Therefore, there is a need to develop active-target fluorescent probes for GBM imaging.

Hence, in this study, we aimed to design and synthesize a novel type of near-infrared fluorescent probe with high inhibitory activity towards the hERG potassium channel, hoping to use this type of probe to systematically explore the therapeutic and imaging potential of the hERG channel and further establish novel strategies for GBM treatment and imaging.

Results and discussion

The design and preparation of near-infrared probes with high binding affinity for the hERG channel

As described above, the hERG potassium channel has been shown to be highly expressed in GBM tumor tissues and can serve as a potential marker and therapeutic target for GBM tumors. Therefore, here we developed a novel type of fluorescent inhibitor of the hERG potassium channel, hoping to offer an innovative treatment strategy for GBM patients (Fig. 1a and b). Simultaneously, probes can also be used for the imaging of GBM tumors and trace the distribution of inhibitors *in vivo*. In the design of the probes, the potent hERG binding ligands astemizole and E4031 were selected as the recognition group, enabling the probes to specifically bind to hERG potassium channels and inhibit their function in tumor cells, finally leading to antitumor efficacy (Fig. 1b). Meanwhile, to increase the depth of penetration and reduce the background signal during imaging, the dye IR780 with near-infrared fluorescence was selected as the fluorescent group. Subsequently, the recognition group and fluorescent group were linked by alkyl chains of different lengths to obtain a series of novel near-infrared hERG potassium channel probes (Fig. 1b), which would be used for GBM tumor imaging and treatment (Fig. 1a).

Subsequently, the designed probes were easily prepared through a substitution reaction between IR780 and the amino-modified hERG ligands astemizole and E4031 in DMF at 80 °C for 2 h (the synthesis procedures are described in the SI file). Afterward, the inhibitory activities of the probes against the hERG channel were evaluated using a radioligand competitive binding assay. The results revealed that all probes had high binding affinities for the hERG channel (Fig. 1c and SI Table S1), with IC_{50} values of 3.62–29.96 nmol. Among them, probe A8, with an eight-carbon linker between IR780 and the piperidine ring, demonstrated the highest activity, with an IC_{50} value of 3.62 nmol. Consequently, probe A8 was selected for further examination of its inhibitory effect on hERG potassium channel function using the manual patch clamp method on CHO cells that stably express hERG potassium channels. As shown in Fig. 1d, upon increasing the concentration of probe A8, the hERG potassium current significantly decreased, and the calculated IC_{50} value is 0.37 μM (Fig. 1e).

The optical properties of the synthesized hERG channel probes and their application in hERG channel imaging

The optical properties of the synthesized hERG channel probes were then measured in various solutions. The results showed that maximum absorption and excitation wavelengths of the probes occur between 630 and 660 nm, with the maximum emission wavelengths typically ranging from 740 to760 nm (Fig. 2a, SI Fig. S1 and Table S2). In addition, the probes possess a substantial Stokes shift of 100 nm, enabling them to effectively mitigate interference from the excitation light on the emission light. Moreover, the probes' emission wavelengths reside in the near-infrared region, which is advantageous for diminishing the background fluorescence signal within

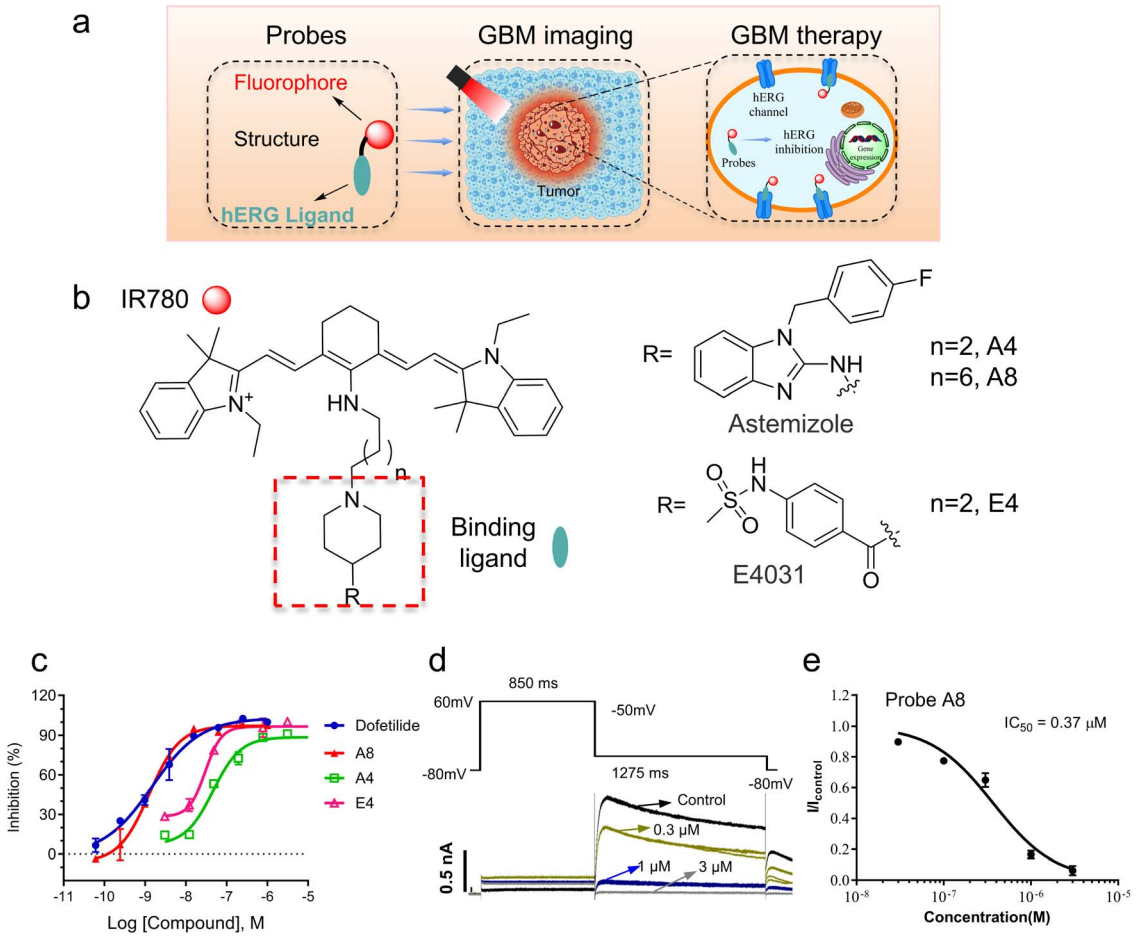

Fig. 1 The design strategy for the novel near-infrared hERG channel probes and testing of their hERG channel binding affinity. (a) A schematic illustration of the imaging and therapy strategies using hERG channel probes. (b) The structures of the designed probes. (c) The inhibition curves for the synthesized probes against the hERG channel determined by radioligand competitive binding assays. The calculated IC_{50} values of the probes are on the nanomolar level, and probe A8 is the best one, with an IC_{50} value of 3.62 nmol. The data are shown as mean ± S.D. values (n = 2). (d) Representative curves showing probe A8 (0.3, 1 and 3 μM) inhibiting the hERG potassium channel tail current. (e) The inhibition curve of probe A8 towards the hERG potassium channel current determined by the manual patch clamp method, with a calculated IC_{50} value of 0.37 μM. The data are shown as mean ± S.D. values (n = 2).

biological systems. As subsequent activity measurements involving the probes are mainly carried out in buffer solution, the fluorescence quantum yields of the probes in PBS were further measured using Cy5 as a reference, and the results are shown in SI Table S1. Compared with probe E4, probes A4 and A8 have higher fluorescence quantum yields, which may be attributed to the electron-donating ability of the nitrogen atom in the astemizole structure. From the above experiments, it can be seen that probe A8 has the highest activity towards hERG potassium channels, alongside superior optical properties, so A8 is selected for further evaluation in subsequent experiments.

In the above experiments, an interesting phenomenon was observed. Compared with organic solvents, the fluorescence intensity of the probes in H_2O and PBS was significantly reduced and the absorption spectra showed a similar trend (Fig. 2a, SI Fig. S1 and Table S2). Because cyanine dyes tend to aggregate in polar solvents, we hypothesized that probes may aggregate in an aqueous environment, such as H_2O or PBS buffer. The results of subsequent dynamic light scattering experiments revealed that A8 does indeed aggregate in saline and PBS buffer at different pH values, with a particle size distribution ranging from 200–1000 nm (Fig. 2b, SI Fig. S3 and Table S3). However, no aggregation phenomenon was observed in organic solvents. Additionally, the lower the pH of the solution, the faster the probe aggregates, which may be due to the increase in positive charge promoting the aggregation of the probe. Then, the morphology of the particles after aggregation of 10 μM A8 in saline was determined using low-magnification transmission electron microscopy, and it was found that A8 can self-aggregate into approximately spherical nanoparticles, with the particle size mainly distributed around 300 nm with a small number of large particles with a size of around 1 μm (SI Fig. S11), which is consistent with the results of dynamic light scattering experiments. To further investigate the aggregation mechanism of A8, UV-vis spectra of A8 in saline were monitored over 4 h, and it was observed that the absorbance of A8 at 640 nm rapidly declined and a new blue-shifted absorption peak appeared at 510 nm (SI Fig. S2a). After A8 was extracted

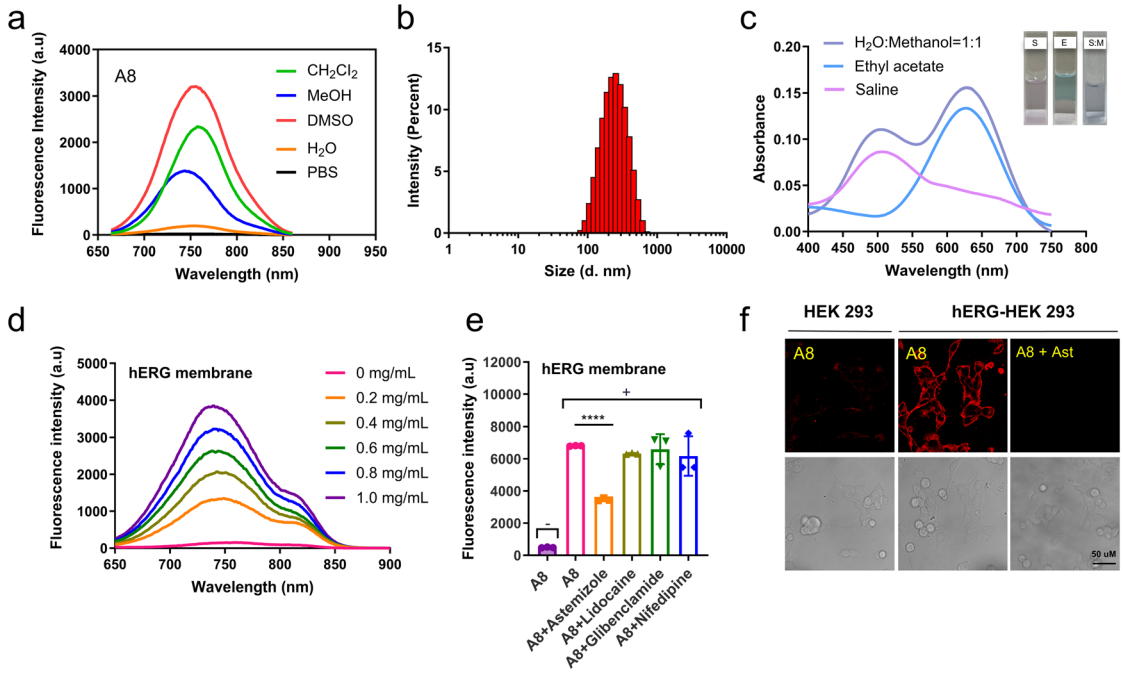

Fig. 2 The properties of the synthesized hERG channel probes and their application in hERG channel imaging. (a) Fluorescence emission spectra of A8 (10 μM) in different solvents. (b) Particle sizes of free A8 in saline determined using a dynamic light scattering instrument. The average particle size is 367 nm. (c) The ultraviolet–visible (UV/vis) absorption spectra of A8 in saline after being left at room temperature for 4 h, in ethyl acetate solution extracted from the above A8 saline solution, and in a H_2O/methanol mixture (1 : 1), respectively. (d) Fluorescence emission spectra of 10 μM A8 incubated with different concentrations of hERG-HEK293 membrane (0, 0.2, 0.4, 0.6, 0.8, and 1.0 mg mL^{-1}) for 30 min at 37 °C. (e) Fluorescence intensity changes of 10 μM probe A8 at the maximum emission wavelength after incubation with 1.0 mg mL^{-1} hERG-HEK293 membrane in the absence or presence of different ion channel inhibitors (hERG channel inhibitor astemizole, sodium ion channel inhibitor lidocaine, ATP-sensitive potassium channel inhibitor glibenclamide, and calcium channel inhibitor nifedipine; 100 μM) for 30 min at 37 °C. The fluorescence intensity of free A8 in assay buffer (no hERG-HEK293 membrane) serves as the background control. The data are shown as mean ± S.D. values ($n = 3$). (f) Representative confocal images of HEK293 cells incubated with 1 μM A8 and hERG-HEK293 cells incubated with 1 μM probe A8 in the presence or absence of 100 μM astemizole; scale bar: 50 μm.

from saline into ethyl acetate, the absorption peak shifted back to 640 nm from 510 nm (Fig. 2c), simultaneously accompanied by a noticeable color change (the inset images in Fig. 2c show the change from pink to blue). This may imply that the absorption peak at 510 nm was not a result of the degradation of the probe, but rather may be due to the conversion of A8 from aggregates to monomers. In addition, in a water–methanol mixture (v/v = 1/1), absorption peaks of A8 at 510 nm and 640 nm can be observed (Fig. 2c), suggesting the coexistence of aggregates and monomers of A8. The effect of aggregation on the optical properties of A8 was then further tested in a water–methanol mixture system at different ratios. It was discovered that the fluorescence intensity of A8 gradually decreased as the proportion of water increased, which might be attributed to aggregation-caused fluorescence quenching effects (SI Fig. S2b).

As A8 has a tendency to aggregate in the aqueous phase, leading to fluorescence quenching and can dissociate into monomers to turn on fluorescence in a hydrophobic environment, we speculated that this fluorescence switch-on mechanism can be applied to selectively label hERG potassium channels with a low background signal.[21,22] The hydrophobic interaction between A8 and the hERG channel may trigger the dissociation of A8 aggregates and activate fluorescence. To validate this hypothesis, probe A8 was incubated with various concentrations of the hERG-transfected HEK293 cell membrane. As illustrated in Fig. 2d, the fluorescence intensity was significantly enhanced as the concentration of the cell membrane increased. When A8 was incubated with 1.0 mg mL^{-1} cell membrane, the fluorescence intensity increased approximately 27-fold compared with the blank control. Thus, probe A8 can successfully light up the hERG channel at a protein molecular level. Subsequently, the fluorescence response selectivity of A8 toward hERG potassium channels was measured by recording the emission spectra of A8 after co-incubation with hERG-HEK293 cell membrane and inhibitors of both the hERG channel and other types of channel (potassium, sodium and calcium ion channels), respectively (Fig. 2e). The results revealed that the fluorescence intensity elevation of A8 induced by incubating with hERG-HEK293 cell membrane can be significantly decreased by astemizole, a potent hERG channel inhibitor. Inhibitors of all other ion channels did not cause a notable change in A8 fluorescence intensity, suggesting that probe A8 can selectively bind to the hERG potassium channel. However, the fluorescence enhancement could not be completely suppressed in the presence of astemizole, possibly due to inevitable nonspecific binding, especially the

hydrophobic component. Given that probe A8 performs well at a molecular level, we further investigated its potential for imaging hERG channels in living cells. Encouragingly, brighter fluorescence signals were observed in hERG-transfected HEK293 cells compared to normal HEK293 cells, and, meanwhile, a significant fluorescence decrease was observed when the cells were co-incubated with probe A8 and astemizole (Fig. 2f). Importantly, a strict washing procedure is not required, making the imaging process very convenient. In conclusion, probe A8 is an excellent imaging reagent for selectively detecting hERG channels.

The antitumor effect of the free hERG channel probe A8 *in vitro*

The experiments above, including radioligand competitive binding assays, patch clamp tests and fluorescence response studies, have shown that probe A8 exhibited potent binding ability toward the hERG potassium channel, and it can effectively inhibit hERG potassium current at the cellular level. As the hERG potassium channel is closely associated with tumor occurrence and development, we further evaluated the anti-GBM tumor activity of A8 at the cellular level. First, the impact of probe A8 on the growth of tumor cells was assessed using the CCK-8 kit on various GBM cell lines (U87/A172/LN229). As shown in Fig. 3a, A8 can effectively inhibit GBM tumor cell proliferation in a dose-dependent manner, with calculated IC_{50} values of about 1 μM. In particular, A8 had a considerably lower effect on the proliferation of normal human astrocyte cells, suggesting lower toxicity toward normal cells and selectivity for tumor cells. Moreover, we examined the antitumor effects of astemizole, IR780 and A8 individually on the U87 cell line. The results revealed that when astemizole and IR780 were connected as a new molecule A8, the anti-proliferative efficacy on tumor cells was enhanced compared to the precursor compounds astemizole and IR780 alone, implying that the design of the probe structure is successful (SI Fig. S4).

Furthermore, the molecular mechanism underlying the antitumor effects of the free hERG channel probe A8 was investigated using transcriptomic sequencing technology (RNA-seq) based on the U87 cell line. In U87 cell proliferation experiments, 3 μM A8 exhibited a strong antitumor effect within 24 h, so this concentration was employed to treat cells in the omics study. The experimental results showed that after U87 cells were treated with A8, a total of 1901 differentially expressed genes (DEGs) were detected at the mRNA level ($\log_2|$ fold change $| \geq 0.8$ and p value < 0.05) compared with the control group, including 787 upregulated genes and 1114 downregulated genes (Fig. 3b and SI Fig. S5a). Functional enrichment of the DEGs was analyzed using the DAVID online analysis tool with the UP_KW biological process and KEGG_pathway categories (Fig. 3c and SI Fig. S5b). The results showed that the downregulated genes were mainly involved in the cellular processes of mitosis, cell cycle, DNA replication and repair, while the upregulated genes were related to cell apoptosis and autophagy (SI Fig. S5c and d). In addition, KEGG_pathway analysis also discovered that the Fanconi anemia pathway was obviously inhibited.

To elucidate the signaling pathway that A8 regulates, in detail, we further analyzed DEGs employing the GSEA online tool with the PID_pathway item. It was found that most of the downregulated DEGs are downstream genes of the transcription factors E2F and FOXM1, or genes involved in PLK1 and Aurora B pathways. E2F and FOXM1 play a crucial role in controlling the transition of the cell cycle from the G1 to the S phase.[23–26] In addition, the components of chromosomal passenger complex (CPC), including AURKB (AuroraB), INCENP, CDCA8, and BIRC5 genes, and its regulatory factors (PLK1 and CDK1) were significantly downregulated by probe A8, which may result in cell mitosis and cell division disorder and inhibit cell proliferation.[27] Therefore, we further tested the effect of probe A8 on the cell cycle in U87 cells. Consistent with the results of the omics studies, treatment with probe A8 indeed resulted in cell arrest in the G0/G1 phase compared to the control group, particularly with a significant decrease in the proportion of cells in the S phase (Fig. 3d). The activity of E2F was regulated by the CDK2-pRB signaling pathway axis. Subsequent western blot analysis showed that CDK2 protein levels were significantly reduced after A8 treatment (Fig. 3e and f), indicating that A8 may inhibit the CDK2-pRB-E2F signaling pathway, thereby downregulating the expression of E2F downstream genes. The genes involved in the Fanconi anemia signaling pathway, including FANCB/D/G/M and FAAP100, were also downregulated.[28] The FA pathway extensively participates in DNA homologous recombination, nucleotide excision and crosslink repair. Thus, the hERG potassium channel may be vital for maintaining the stability of the genome in response to genotoxic insults. The upregulated genes related to apoptosis consist of both pro-apoptotic (BCL10 and CASP3) and anti-apoptotic (BAG1 and BCL2A1) genes. However, cell apoptosis is regulated by a complex network, and nuclear staining with Hoechst revealed that cells treated with 3 μM A8 displayed marked nuclear pyknosis (SI Fig. S6), suggesting that the ultimate result of probe A8's action is to induce cell apoptosis. Moreover, there was significant upregulation of some autophagy markers, such as MAP1LC3B2, MAP1LC3B, and ATG4B.[29,30] The cell morphology was then analyzed using transmission electron microscopy (TEM), and numerous autophagosomes were observed in the A8 treatment group (Fig. 3g), indicating A8 can induce significant cellular autophagy. Interestingly, genes associated with endoplasmic reticulum (ER) stress induced by unfolded proteins, such as ATF4, ERN1, and XBP1, were upregulated.[31] Western blot analysis confirmed that ATF4 protein expression was significantly enhanced after A8 treatment (Fig. 3h and i). Therefore, it is speculated that cell apoptosis and cell autophagy may be caused by ER stress. It has been reported that certain hERG mutations can impair the trafficking of hERG, leading to its retention in ER and subsequent ER stress.[32] Some hERG channel inhibitors can also impede hERG potassium channels in the ER by interacting with Tyr652 and Phe656 residues.[33] It is speculated that compound A8 may have a similar effect. Immunofluorescence colocalization analysis in hERG-U87 cells, which highly express the hERG potassium channel, demonstrated that A8 treatment

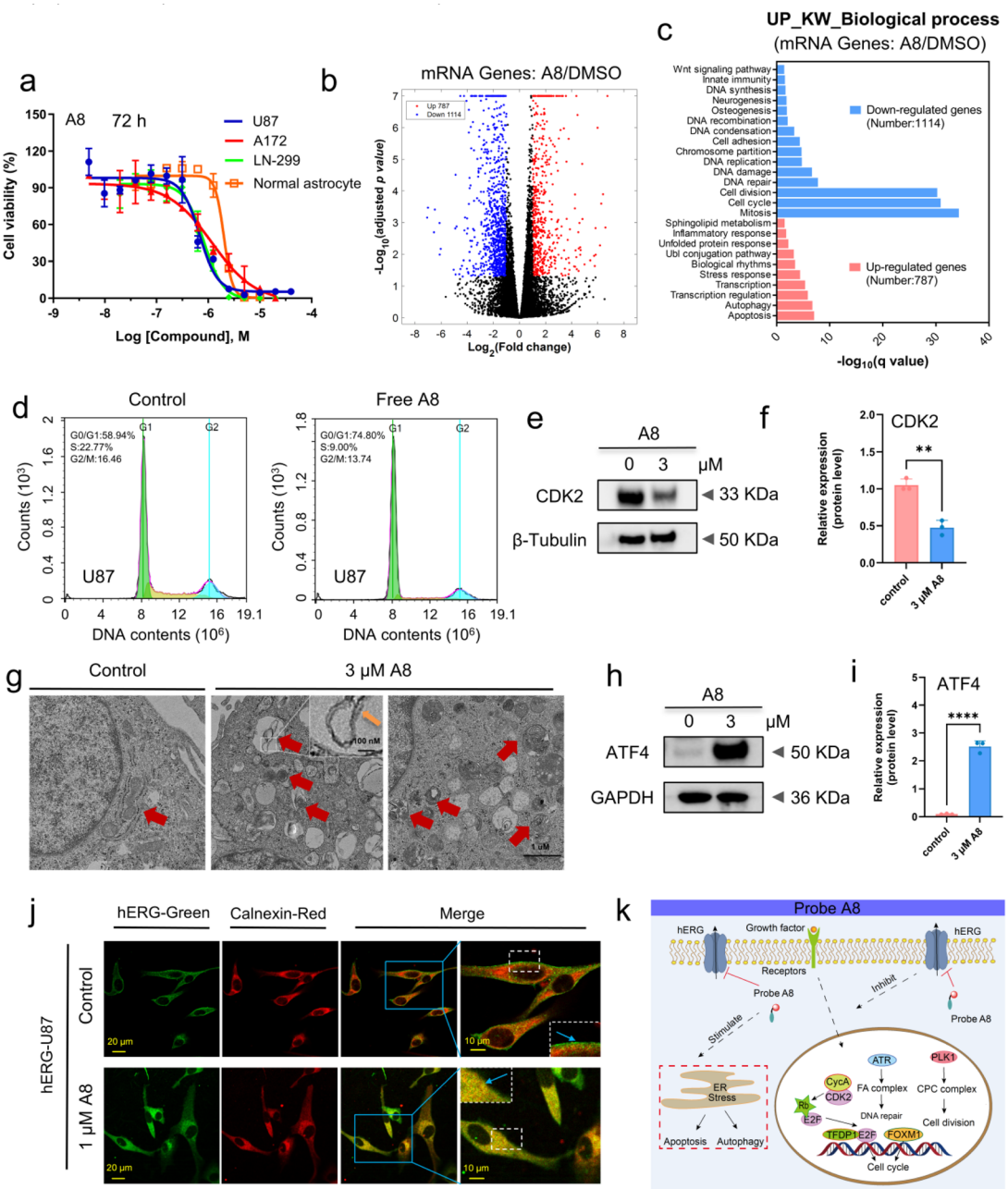

Fig. 3 The antitumor effects of free hERG channel probe A8 in vitro. (a) The dose-dependent inhibition curves of A8 toward the growth of various GBM tumor cells (U87, A172 and T98G). Data are shown as mean ± S.D. values ($n = 3$). (b) A volcano plot of the transcriptomics results from U87 cells after treatment with A8 or vehicle (DMSO); differentially expressed genes (DEGs, $\log_2|\text{fold change}| \geq 0.8$ and p value < 0.05) are plotted with blue (down-regulated genes) or red (upregulated genes) dots. (c) Functional enrichment analysis of DEGs using the DAVID online tool with UP_KW biological process categories. (d) Cell cycle analysis of U87 cells after treatment with vehicle (DMSO, control group) or 0.3 μM A8 for 24 h. DNA was stained with PI and then analyzed by flow cytometry. Western blot (e) and the corresponding quantitative (f) analysis of CDK2 expression in U87 cells after treatment with A8 or vehicle (DMSO) for 24 h (data are shown as mean ± S.D. values ($n = 3$)). (g) Transmission electron microscope images of U87 cells after treatment with A8 (3 μM) or vehicle (DMSO); magnification: 8500×. Obvious autophagy was observed in the A8 treatment group; the red arrows indicate autophagosomes, and some of them contain ER membranes (brown arrows: ribosomes can be observed; the white lines indicate the magnified area (scale bar: 100 nm)); scale bar: 1 μm. Western blot (h) and the corresponding quantitative (i) analysis of ATF4 expression in U87 cells after treatment with A8 (3 μM) or vehicle (DMSO) for 24 h (data are shown as mean ± S.D. values ($n = 3$)). (j) Immunofluorescence colocalization analysis of the hERG channel and ER marker calnexin in hERG-U87 cells after treatment with A8 (1 μM) or vehicle (control, DMSO) for 24 h. The hERG channel exhibited reduced cell membrane distribution and was highly colocalized with the ER marker calnexin after treatment with 1 μM A8 in hERG-U87 cells. (k) A summary of the major signal pathways that were influenced by A8 in the U87 glioblastoma cell line. RB-E2F, FOXM1, chromosomal passenger complex (CPC) and Fanconi anemia signal pathways were significantly suppressed by A8, and apoptosis and autophagy mediated by endoplasmic reticulum stress were significantly upregulated.

diminished hERG localization in the plasma membrane while increasing its distribution in the ER (Fig. 3j), verifying the hypothesis. ER phagocytosis was also observed in TEM imaging (Fig. 3g). Collectively, it can be concluded that hERG inhibition by A8 can lead to the retention of hERG channel in the ER, triggering ER stress and subsequently inducing autophagy and apoptosis (Fig. 3k).

The preparation and characterization of the ApoE peptide-modified liposome ApoE-Lipo@A8

It has been established that A8 can produce potent antitumor activity in in vitro GBM cell lines. However, hERG channel inhibition by A8 has the risk of causing cardiac toxicity, which may impede its application *in vivo*. In addition, for a probe to achieve both the treatment and imaging of brain tumors, it must be able to cross the blood–brain barrier. To address these issues, we encapsulated A8 in liposomes, hoping to increase the GBM tumor targeting and reduce the possible toxicity of A8. In the design of the liposome, PC (phosphatidylcholine) and CH (cholesterol) are the basic materials (Fig. 4a). To further enhance the drug delivery efficiency to orthotopic glioblastoma tissues, DSPE-PEG2000, DSPE-PEOz, and DSPE-PEG2000-ApoE were also incorporated into the membrane structure of the liposomes (Fig. 4a). DSPE-PEG2000 and DSPE-PEOz, as long-circulation materials, can increase the stability of the liposomes *in vivo*. ApoE can target a variety of low-density lipoprotein receptors (*e.g.*, LDLR, LRP1, and LRP2) that are overexpressed in endothelial cells at the blood–brain barrier and basement membrane cells, mediating endocytosis to help the liposomes cross the blood–brain barrier efficiently.[34]

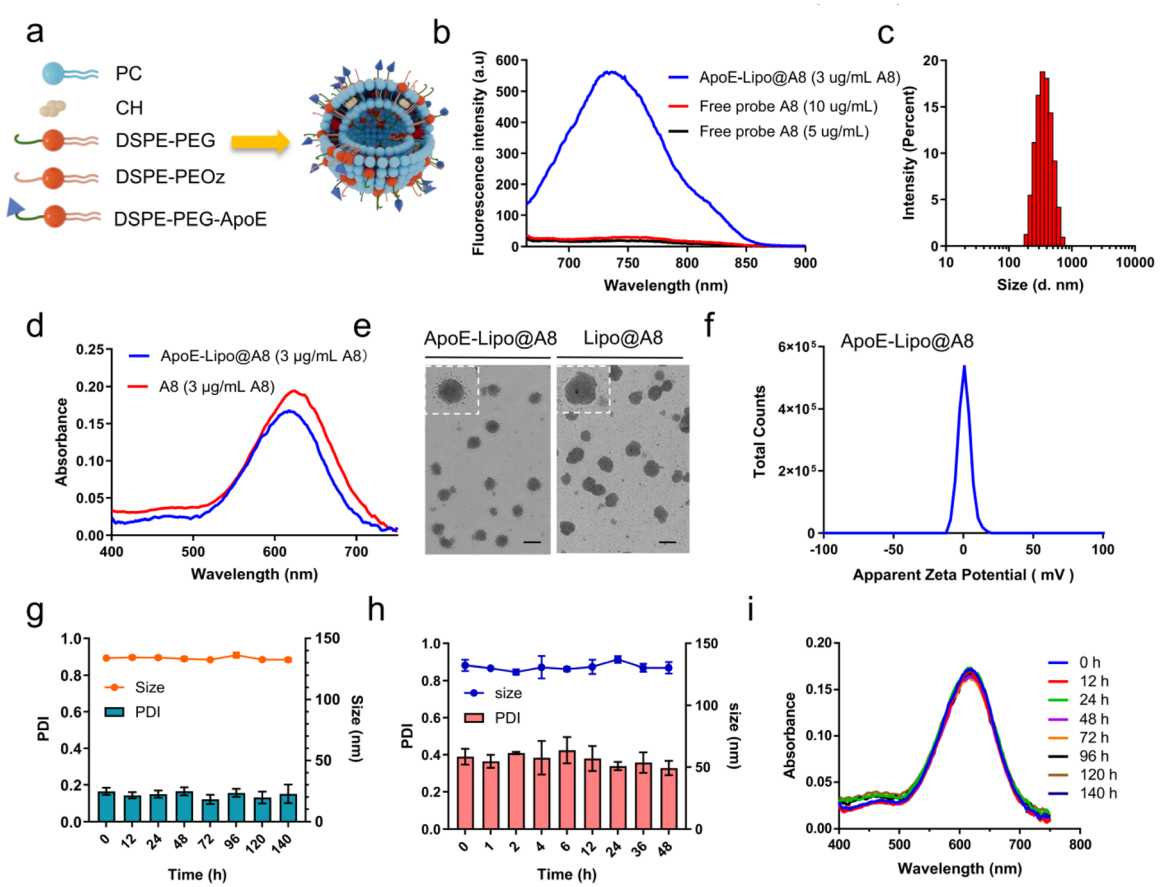

Fig. 4 Characterization of hERG-probe-encapsulating ApoE-Lipo@A8 liposomes. (a) A schematic diagram of the structure of the designed liposome ApoE-Lipo@A8. PC and CH are the basic materials, and DSPE-PEG2000, DSPE-PEOz, and DSPE-PEG2000-ApoE confer the liposome ApoE-Lipo@A8 with the properties of stability and the ability to cross the blood–brain barrier. A8 was loaded in the lipid layer. (b) Fluorescence emission spectra of free probe A8 (5 μg mL^{-1} and 10 μg mL^{-1}) and ApoE-Lipo@A8 (3 μg mL^{-1} A8) (Ex = 644 nm) in saline. (c) The particle sizes of liposome ApoE-Lipo@A8 determined by dynamic light scattering assays. The average size of ApoE-Lipo@A8 is 132.9 ± 1.5 nm (mean ± S.D., n = 3, PDI < 0.2). (d) The absorption spectra of free probe A8 (3 μg mL^{-1}) and ApoE-Lipo@A8 (containing 3 μg mL^{-1} A8) (Ex = 644 nm) in water. (e) Representative low-magnification transmission electron microscopy (TEM) images of ApoE-Lipo@A8 and Lipo@A8 (without the incorporation of DSPE-PEG2000-ApoE). (f) The zeta potential of ApoE-Lipo@A8 determined by dynamic light scattering assays. (g) Changes in the particle size and PDI of ApoE-Lipo@A8 over 140 h under storage conditions (4 °C). No significant changes were observed and ApoE-Lipo@A8 exhibited good colloidal stability. Data are shown as mean ± S.D. values (n = 3). (h) Changes in the particle size and PDI of ApoE-Lipo@A8 in DMEM supplemented with 10% serum over 60 h at 37 °C. No significant alterations were observed and ApoE-Lipo@A8 showed good colloidal stability under simulated physiological conditions. Data are shown as mean ± S.D. values (n = 3). (i) The UV-visible absorption spectra of ApoE-Lipo@A8 (100 μg mL^{-1}) over 140 h at 4 °C.

Subsequently, the designed ApoE-Lipo@A8 liposomes were prepared through a thin-film dispersion and ApoE post-insertion method. Probe A8 was loaded in the lipid layer. Subsequent UV–vis absorption and fluorescence emission spectra of ApoE-Lipo@A8 showed absorption and emission peaks at 621 nm and 735 nm, respectively, which are consistent with those of free A8, indicating the successful encapsulation of A8 within ApoE-Lipo@A8 (Fig. 4b and d). Additionally, it was observed that the fluorescence intensity of A8 significantly increased after encapsulation in the liposomes (Fig. 4b), which may be because A8 is uniformly dispersed in the phospholipid bilayer of the liposomes, avoiding aggregation-caused fluorescence quenching of probe A8. The encapsulation efficiency (EE) and loading efficiency (LE) of A8 in ApoE-Lipo@A8 were determined to be 86.37% and 2.43%, respectively.

The diameter, uniformity, and zeta potential of ApoE-Lipo@A8 have a great impact on its efficacy, so these three parameters were measured using a dynamic light scattering instrument. As depicted in Fig. 4c, the average size of ApoE-Lipo@A8 is 132.9 $\pm$ 1.5 nm, and the distribution is uniform (PDI < 0.2). This particle size range is conducive to the enrichment of liposomes at the tumor site through the EPR effect, thereby improving the efficacy. The particle size of Lipo@A8 without being modified with the ApoE-targeting peptide was 129.0 $\pm$ 1.2 nm (SI Fig. S7a), slightly smaller than that of ApoE-Lipo@A8 liposomes, which may be due to surface modification by targeting peptides of the liposomes. The zeta potential of ApoE-Lipo@A8 liposomes was 4.6 $\pm$ 0.3 mV (Fig. 4f), indicating that ApoE-Lipo@A8 is a cationic liposome, which facilitates its uptake by cells with negatively charged surfaces due to phosphate groups. The zeta potential of Lipo@A8 was 7.8 $\pm$ 0.2 mV (SI Fig. S7b), slightly higher than that of ApoE-Lipo@A8, suggesting that modification with ApoE may reduce the positive charge on the surface of the liposomes. Afterwards, the morphologies of ApoE-Lipo@A8 and Lipo@A8 were imaged *via* transmission electron microscopy (TEM). As shown in Fig. 4e, both ApoE-Lipo@A8 and Lipo@A8 were uniform spherical particles with a particle size of about 130 nm. In comparison to Lipo@A8, ApoE-Lipo@A8 liposomes were uniformly surrounded by a large number of small black particles around the periphery. These particles might be ApoE peptides adsorbed onto the surface of the liposomes. The results of the experiments above also confirmed that the targeting peptide ApoE has been successfully modified on the surface of ApoE-Lipo@A8 liposomes, thereby ensuring a brain-targeting effect, allowing ApoE-Lipo@A8 to cross the blood–brain barrier. The stability of liposomes is pivotal for drug efficacy. Hence, the colloidal stability of ApoE-Lipo@A8 was then measured. The experimental results illustrated that there were no obvious alterations in the average particle size of ApoE-Lipo@A8 and its PDI values for up to 140 h at 4 °C (Fig. 4g), demonstrating that ApoE-Lipo@A8 is stable for a long time without rupturing or aggregating under these storage conditions. Moreover, DMEM culture medium supplemented with 10% serum was used to simulate physiological conditions. As described in Fig. 4h, in this environment, the particle size and PDI of ApoE-Lipo@A8 fluctuated less over 60 h. Thus, A8 might be stable in the blood circulation system and could be administered *via* intravenous injection. Meanwhile, the absorption spectra of liposomes held steady for a duration of 140 h at 4 °C (Fig. 4i), which suggested that A8 remains very stable after loading onto liposomes.

As described above, free A8 exhibited good antitumor activity. Whether this activity can be maintained upon loading onto liposomes needs to be confirmed. Therefore, the *in vitro* anticancer efficacy of ApoE-Lipo@A8 was examined by the CCK-8 assay in U87 cells. As shown in SI Fig. S8, lower concentrations of ApoE-Lipo@A8 can exhibit strong antitumor effects, with a calculated IC_{50} value of approximately 1 μM (converted from the drug loading amount to the concentration of probe A8), which is comparable to the free probe A8.

In vivo imaging with ApoE-Lipo@A8

To evaluate the tumor-targeting ability of ApoE-Lipo@A8 *in vivo*, we administered ApoE-Lipo@A8 *via* the tail vein to orthotopic U87-Luc tumor-bearing mice and normal mice. Then, fluorescence imaging of the mice was performed at different time points using an IVIS® Lumina III (PerkinElmer) imaging system. As shown in Fig. 5a, compared with the normal group, significant fluorescence was observed at the tumor location in the brain of U87 tumor-bearing mice, indicating that ApoE-Lipo@A8 could effectively penetrate the blood–brain barrier and accumulate at the tumor site. The fluorescence gradually diminished after 6 h, potentially due to drug metabolism. After 48 h of imaging, the mice were euthanized, and the brains were harvested for imaging. Strong fluorescence signals still could be detected from the tumor tissue, while no obvious fluorescence signals were recorded from the healthy brain tissue region of the tumor-bearing mice or from the brains of normal mice (Fig. 5b and c). Notably, compared to the free A8 administration group, encapsulating A8 in ApoE-Lipo@A8 liposomes enables it to effectively cross the blood–brain barrier and target tumors (Fig. 5f). Thus, the designed liposome drug delivery system is successful and can help A8 to reach orthotopic tumors, which is important for antitumor activity *in vivo*. The tumor-targeting properties also make ApoE-Lipo@A8 suitable for GBM tumor imaging. Furthermore, the major organs were also isolated, and it was found that both the ApoE-Lipo@A8 liposomes and free A8 were distributed more in the liver, lungs, spleen, and kidneys (Fig. 5d and e), which may be related to their metabolic pathway. Meanwhile, lower accumulation in the heart may suggest a potentially favorable cardiac safety profile. Furthermore, organs from the free-probe group showed lower fluorescence intensity than those from the liposome group. This might be because the free probe is cleared more quickly *in vivo*, whereas encapsulating the probe into liposomes enhances its metabolic stability. Additionally, compared to the free probe group, the distribution of ApoE-Lipo@A8 in the lungs increased after intravenous injection. This phenomenon is likely attributable to the liposomes' slightly positive charge (zeta potential: 4.6 $\pm$ 0.3 mV), which promotes electrostatic adsorption onto the negatively charged luminal surface of pulmonary vascular endothelial cells,[35] thereby enhancing the pulmonary

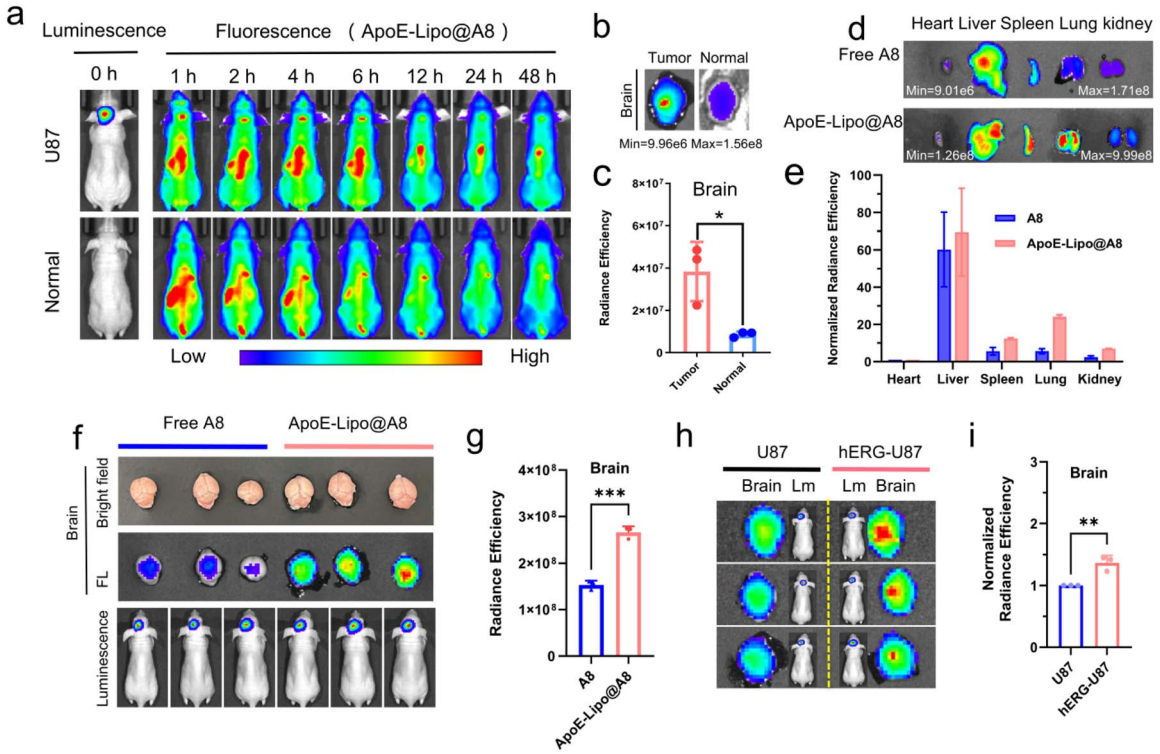

Fig. 5 *In vivo* imaging with ApoE-Lipo@A8. (a) Representative *in vivo* fluorescence images of orthotopic U87-Luc tumor-bearing mice after the intravenous injection of ApoE-Lipo@A8 (3 mg kg^{-1}) (Ex = 640 nm; Em = 760 nm). The left column shows bioluminescence images of U87-Luc orthotopic xenografts. Representative fluorescence images (b) and the fluorescence intensity histogram (c, mean ± S.D., $n = 3$, $^{*}p < 0.05$) of brains isolated from tumor-bearing mice (U87-Luc) 48 h after the administration of ApoE-Lipo@A8 (Ex = 640 nm; Em = 760 nm). ApoE-Lipo@A8 can selectively accumulate at the tumor sites. Representative fluorescence images (d) and the normalized fluorescence intensity histogram (e) of major organs isolated from tumor-bearing mice (U87-Luc) 6 h after the administration of free A8 and ApoE-Lipo@A8 (Ex = 640 nm; Em = 760 nm). The fluorescence intensities of all organs were normalized to that of the heart. Fluorescence images (f) and fluorescence intensities (g, mean ± S.D., $n = 3$, $^{***}p < 0.001$) of brains harvested from tumor-bearing mice (U87-Luc) 6 h after the administration of free A8 and ApoE-Lipo@A8 (Ex = 640 nm; Em = 760 nm). The bottom row in (f) shows bioluminescence images of U87-Luc orthotopic xenografts. Fluorescence images (h) and the fluorescence intensity histogram (i, mean ± S.D., $n = 3$, $^{**}p < 0.01$) of brains isolated from U87-Luc or hERG-U87-Luc tumor-bearing mice 48 h after the administration of ApoE-Lipo@A8 (Ex = 640 nm; Em = 760 nm). The fluorescence intensity of the hERG-U87-Luc group was normalized to the U87-Luc group.

accumulation of ApoE-Lipo@A8. Despite the higher levels of lung accumulation, hematoxylin and eosin (H&E) staining of lung tissue following a single ApoE-Lipo@A8 treatment cycle revealed no discernible histopathological abnormalities, suggesting a favorable pulmonary tolerability profile (SI Fig. S9). To further validate whether the probe can be used for the *in vivo* imaging of hERG potassium channels, an orthotopic brain tumor model was established using hERG-U87 cells. As depicted in Fig. 5h and i, strong fluorescence intensity was observed in tumors with high hERG expression, suggesting that probe A8 can effectively bind to hERG channels and be used for their imaging *in vivo*.

In vivo antitumor effects of ApoE-Lipo@A8

As ApoE-Lipo@A8 can efficiently accumulate in GBM tumors, the antitumor efficacy of ApoE-Lipo@A8 was next evaluated in orthotopic U87 MG-Luc GBM xenografts (Fig. 6a). 10 days after tumor implantation, the tumor-bearing nude mice were randomly divided into two groups. They were treated with PBS (control group) and ApoE-Lipo@A8 (dose: 3 mg kg^{-1}), respectively. ApoE-Lipo@A8 was administered *via* tail vein injection every other day for a total of five doses. Then, tumor growth was monitored by *in vivo* bioluminescence imaging and quantified based on relative photon flux. As shown in Fig. 6c, d and f, ApoE-Lipo@A8 effectively inhibited intracranial tumor growth. After finishing the treatment cycle, the mice were euthanized, and their brains and major organs were harvested. Hematoxylin and eosin (H&E) staining analysis of the harvested brains confirmed that the ApoE-Lipo@A8 treatment group achieved effective tumor suppression with reduced tumor volume compared with the PBS group (Fig. 6e). TUNEL assay and Ki-67 staining analysis of the tumor tissues showed that ApoE-Lipo@A8 liposomes significantly induced tumor cell apoptosis and inhibited tumor cell proliferation (Fig. 6h and i). More importantly, Kaplan–Meier survival curves showed that ApoE-Lipo@A8 markedly increased the survival times of mice, with a median survival time of 48 d, twice that of the PBS group (Fig. 6g).

Safety is a critical consideration for the clinical use of drugs, which must demonstrate not only strong therapeutic efficacy

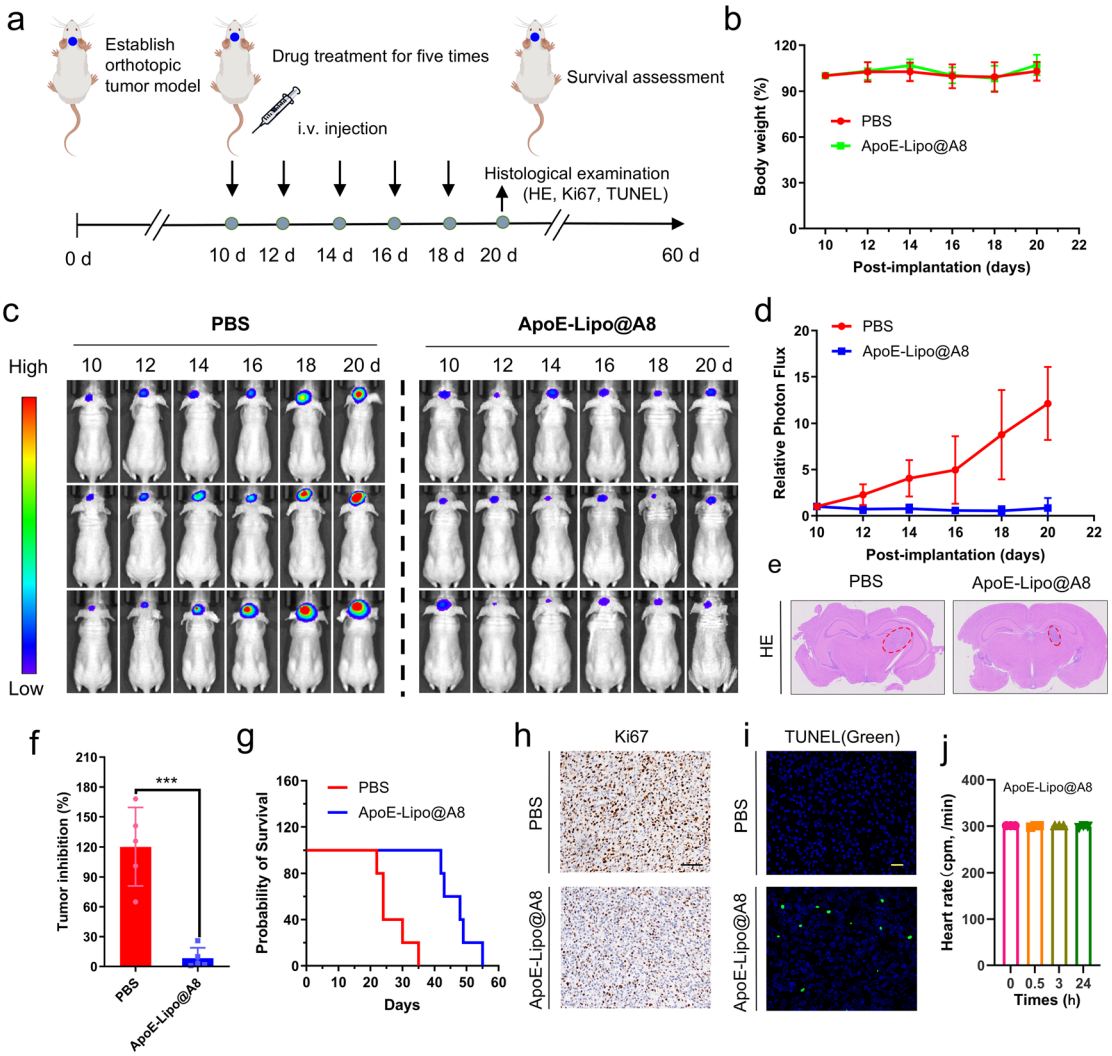

Fig. 6 The *in vivo* antitumor activity of ApoE-Lipo@A8. (a) The experimental setup for the treatment of GBM tumors with ApoE-Lipo@A8. Nude mice were orthotopically implanted with U87 glioblastoma cells. From the 10th day after tumor implantation, ApoE-Lipo@A8 was administered *via* the tail vein every other day for a total of five doses. After one cycle of treatment was completed, mice were euthanized and tumor tissues were isolated for further H&E, Ki67 and TUNEL staining analysis. (b) The bodyweight changes of mice treated with vehicle (PBS) or ApoE-Lipo@A8 over the treatment period; data are shown as mean ± S.D. values ($n = 5$). (c) Representative bioluminescence images of glioblastoma orthotopic xenografts at each treatment point. (d) The tumor size changes of mice treated with vehicle (PBS) or ApoE-Lipo@A8 over the treatment period. Tumor sizes were reflected by the bioluminescence intensities of orthotopic xenograft tumors and plotted relative to the baseline bioluminescence on the 10th day. Data are shown as mean ± S.D. values ($n = 5$). (e) Representative H&E staining results of brain tissues excised from vehicle (PBS)- or Apo-Lipo@A8-treated mice. (f) The tumor inhibition rate after finishing one cycle of treatment with ApoE-Lipo@A8 (mean ± S.D., $n = 5$); ***$p < 0.01$. The tumor size of the vehicle (PBS) group was plotted as 1. (g) Survival statistics of mice after one treatment cycle. ApoE-Lipo@A8 treatment can significantly increase the survival rate of tumor-bearing mice. (h) Representative immunohistochemical staining of Ki-67 in tumor tissues excised from vehicle (PBS)- or ApoE-Lipo@A8-treated mice; scale bar: 100 μm. (i) Representative apoptotic staining images (TUNEL, scale bar: 20 μm) of tumor tissues that were excised from vehicle (PBS)- or ApoE-Lipo@A8-treated mice. (j) Heart rate changes over 24 hours after the administration of ApoE-Lipo@A8.

but also minimal toxicity. During the treatment period, there were no significant changes in the body weights of mice (Fig. 6b), and other abnormal symptoms also did not appear, suggesting that drug treatment did not cause adverse effects. To further investigate the safety of the drug, H&E staining of the major organs was carried out. The results showed that ApoE-Lipo@A8 had no significant toxic side effects on the heart, liver, spleen, lungs, and kidneys after one treatment cycle (SI Fig. S9). Therefore, the liposome ApoE-Lipo@A8 has low toxicity when applied in the treatment of GBM tumors. Moreover, heart rates were monitored for 24 hours after ApoE-Lipo@A8 administration, and no acute abnormalities in heart rate were observed, indicating low cardiac toxicity (Fig. 6j).

Conclusions

In this study, we developed a novel near-infrared fluorescent probe A8 targeting the hERG channel. The results of radioligand

competitive binding assays and patch clamp experiments showed that probe A8 exhibited high binding affinity towards the hERG channel with IC_{50} values of 3.62 nmol and 0.37 μM, respectively. Using this probe, the therapeutic and imaging potential of the hERG channel for glioblastoma was systematically explored.

After a series of evaluations, it was found that suppressing the hERG channel using A8 can induce significant tumor suppression activity at the molecular, cellular and *in vivo* levels. The survival rates of mice bearing orthotopic GBM xenografts were greatly improved after treatment with A8 compared with the control group. It is worth noting that to achieve the *in vivo* application of A8, probe A8 was encapsulated into a novel ApoE-modified liposome, ApoE-Lipo@A8, which incorporated brain vascular endothelial cell-targeting peptide ApoE-modified DSPE-PEG2000, DSPE-PEG2000 and DSPE-PEOz. Subsequent *in vivo* fluorescence imaging with A8 confirmed that this delivery system effectively helped A8 to better penetrate the blood–brain barrier and accumulate at the tumor site compared to the free A8 probe after intravenous injection. Meanwhile, both free A8 and ApoE-Lipo@A8 exhibited a low cardiac distribution, suggesting potentially reduced cardiotoxicity, which is very important for hERG channel inhibitors for cancer therapy. Moreover, no abnormalities in heart rate were observed after treatment with ApoE-Lipo@A8. This may provide a convenient formulation method to address the challenges faced by hERG channel inhibitors for GBM treatment (the blood–brain barrier and cardiac toxicity). Additionally, unbiased omics studies also unveiled a novel molecular mechanism underlying the anti-tumor effects of hERG channel inhibition, including inhibiting the CDK2-pRB-E2F and Fanconi anemia signaling pathways and triggering ER-stress-dependent apoptosis and autophagy. This valuable pharmacological information relating to A8's action in glioblastoma cells may aid further drug development of hERG channel inhibitors for cancer therapy.

Probe A8 can selectively label the hERG channel based on the ACQ (aggregation-caused quenching) effect, and it can be used for hERG channel imaging at cellular and *in vivo* levels, and further for GBM tumor imaging. In a previous study, Li's and Wang's groups developed a series of hERG channel probes using a PET (intramolecular photoinduced electron transfer), environment-sensitive, AIE or molecular-rotation fluorescence turn on mechanism.[36–40] However, the fluorescence emission wavelengths of these probes were short, and they were only used for cellular imaging of the hERG channel. This is the first time exploring the *in vivo* imaging of the hERG channel using a fluorescent probe.

In conclusion, our study developed a novel near-infrared hERG channel probe A8 with lower toxicity that can be used for GBM therapy and imaging. This work established a promising strategy for GBM therapy and imaging, which would promote the development of the hERG channel as a cancer therapeutic target. Meanwhile, the hERG potassium channel is implicated in multiple signaling pathways, and hERG innervation by probe A8 also holds great potential for combination therapies with other treatment methods, such as immunotherapy, radiotherapy, or targeted agents, to overcome the therapeutic resistance or heterogeneity of GBM, ultimately improving patient outcomes.

Ethical statement

All animal experiments were performed in compliance with the relevant guidelines and regulations of the People's Republic of China for the care and use of experimental animals (Regulations on the Administration of Laboratory Animals of the People's Republic of China, *etc.*). All animal procedures were performed in accordance with the Guidelines for the Care and Use of Laboratory Animals of Shandong Normal University and approved by the Animal Ethics Committee of Shandong Normal University (AEECSDNU2022025).

Author contributions

Conception and design: Zhenzhen Liu, Ping Li, Bo Tang. Development of methodology: Zhenzhen Liu, Li Liu, Tongtong Ban. Acquisition of data (provided animals, provided facilities, *etc.*): Zhenzhen Liu, Li Liu, Tongtong Ban, Ruihao Li, Xiao Zhang, Yuanwen Wang, Xiaojuan Li. Analysis and interpretation of data (*e.g.*, statistical analysis, biostatistics, computational analysis): Zhenzhen Liu, Li Liu, Tongtong Ban, Ruihao Li, Xiao Zhang, Yuanwen Wang, Xiaojuan Li. Writing, review, and/or revision of the manuscript: Zhenzhen Liu, Li Liu, Tongtong Ban, Ping Li, Bo Tang. Administrative, technical, or material support (*i.e.*, reporting or organizing data, constructing databases): Zhenzhen Liu, Ping Li, Bo Tang, Xin Wang, Wei Zhang. Study supervision: Zhenzhen Liu, Ping Li, Bo Tang.

Conflicts of interest

No potential conflicts of interest are disclosed.

Data availability

The data supporting this article have been included as part of the supplementary information (SI). Supplementary information: the general information, methods, NMR spectra, MS spectra, synthetic details, biological details. The differentially expressed genes (DEGs) that were identified through RNA sequencing (RNA-seq) are shown in supplementary excel files. See DOI: **https://doi.org/10.1039/d5sc05222j**.

Acknowledgements

This work was supported by the National Natural Science Foundation of China (21907061, 22134004, 22304107, and 22377070) and the Natural Science Foundation of Shandong Province of China (ZR2023ZD31, ZR2023YQ016).

Notes and references

1 M. Preusser, M. Lim, D. A. Hafler, D. A. Reardon and J. H. Sampson, Prospects of immune checkpoint

modulators in the treatment of glioblastoma, *Nat. Rev. Neurol.*, 2015, **11**, 504–514.
2 M. Westphal and K. Lamszus, The neurobiology of gliomas: from cell biology to the development of therapeutic approaches, *Nat. Rev. Neurosci.*, 2011, **12**, 495–508.
3 A. S. Modrek, N. S. Bayin and D. G. Placantonakis, Brain stem cells as the cell of origin in glioma, *World J. Stem Cells*, 2014, **6**, 43–52.
4 G. Yan, Y. Wang, J. Chen, W. Zheng, C. Liu, S. Chen, L. Wang, J. Luo and Z. Li, Advances in drug development for targeted therapies for glioblastoma, *Med. Res. Rev.*, 2020, **40**, 1950–1972.
5 D. A. Reardon, A. A. Brandes, A. Omuro, P. Mulholland, M. Lim, A. Wick, J. Baehring, M. S. Ahluwalia, P. Roth, O. Bähr, S. Phuphanich, J. M. Sepulveda, P. De Souza, S. Sahebjam, M. Carleton, K. Tatsuoka, C. Taitt, R. Zwirtes, J. Sampson and M. Weller, Effect of Nivolumab vs Bevacizumab in Patients With Recurrent Glioblastoma: The CheckMate 143 Phase 3 Randomized Clinical Trial, *JAMA Oncol.*, 2020, **6**, 1003–1010.
6 M. Lim, Y. Xia, C. Bettegowda and M. Weller, Current state of immunotherapy for glioblastoma, *Nat. Rev. Clin. Oncol.*, 2018, **15**, 422–442.
7 N. Hilf, S. Kuttruff-Coqui, K. Frenzel, V. Bukur, S. Stevanović, C. Gouttefangeas, M. Platten, G. Tabatabai, V. Dutoit, S. H. van der Burg, P. Thor Straten, F. Martínez-Ricarte, B. Ponsati, H. Okada, U. Lassen, A. Admon, C. H. Ottensmeier, A. Ulges, S. Kreiter, A. von Deimling, M. Skardelly, D. Migliorini, J. R. Kroep, M. Idorn, J. Rodon, J. Piró, H. S. Poulsen, B. Shraibman, K. McCann, R. Mendrzyk, M. Löwer, M. Stieglbauer, C. M. Britten, D. Capper, M. J. P. Welters, J. Sahuquillo, K. Kiesel, E. Derhovanessian, E. Rusch, L. Bunse, C. Song, S. Heesch, C. Wagner, A. Kemmer-Brück, J. Ludwig, J. C. Castle, O. Schoor, A. D. Tadmor, E. Green, J. Fritsche, M. Meyer, N. Pawlowski, S. Dorner, F. Hoffgaard, B. Rössler, D. Maurer, T. Weinschenk, C. Reinhardt, C. Huber, H. G. Rammensee, H. Singh-Jasuja, U. Sahin, P. Y. Dietrich and W. Wick, Actively personalized vaccination trial for newly diagnosed glioblastoma, *Nature*, 2019, **565**, 240–245.
8 S. J. Bagley, M. Logun, J. A. Fraietta, X. Wang, A. S. Desai, L. J. Bagley, A. Nabavizadeh, D. Jarocha, R. Martins, E. Maloney, L. Lledo, C. Stein, A. Marshall, R. Leskowitz, J. K. Jadlowsky, S. Christensen, B. S. Oner, G. Plesa, A. Brennan, V. Gonzalez, F. Chen, Y. Sun, W. Gladney, D. Barrett, M. P. Nasrallah, W. T. Hwang, G. L. Ming, H. Song, D. L. Siegel, C. H. June, E. O. Hexner, Z. A. Binder and D. M. O'Rourke, Intrathecal bivalent CAR T cells targeting EGFR and IL13Rα2 in recurrent glioblastoma: phase 1 trial interim results, *Nat. Med.*, 2024, **30**, 1320–1329.
9 M. H. Noh, J. M. Kang, A. A. Miller, G. Nguyen, M. Huang, J. S. Shim, A. J. Bueso-Perez, S. A. Murphy, K. A. Rivera-Caraballo, Y. Otani, E. Kim, S. H. Yoo, Y. Yan, Y. Banasavadi-Siddegowda, H. Nakashima, E. A. Chiocca, B. Kaur, Z. Zhao, T. J. Lee and J. Y. Yoo, Targeting IGF2 to reprogram the tumor microenvironment for enhanced viro-immunotherapy, *Neuro-Oncology*, 2024, **26**, 1602–1616.
10 M. C. Trudeau, J. W. Warmke, B. Ganetzky and G. A. Robertson, HERG, a human inward rectifier in the voltage-gated potassium channel family, *Science*, 1995, **269**, 92–95.
11 G. A. Smith, H. W. Tsui, E. W. Newell, X. Jiang, X. P. Zhu, F. W. Tsui and L. C. Schlichter, Functional up-regulation of HERG K+ channels in neoplastic hematopoietic cells, *J. Biol. Chem.*, 2002, **277**, 18528–18534.
12 E. Afrasiabi, M. Hietamäki, T. Viitanen, P. Sukumaran, N. Bergelin and K. Törnquist, Expression and significance of HERG (KCNH2) potassium channels in the regulation of MDA-MB-435S melanoma cell proliferation and migration, *Cell. Signalling*, 2010, **22**, 57–64.
13 E. Lastraioli, L. Guasti, O. Crociani, S. Polvani, G. Hofmann, H. Witchel, L. Bencini, M. Calistri, L. Messerini, M. Scatizzi, R. Moretti, E. Wanke, M. Olivotto, G. Mugnai and A. Arcangeli, herg1 gene and HERG1 protein are overexpressed in colorectal cancers and regulate cell invasion of tumor cells, *Cancer Res.*, 2004, **64**, 606–611.
14 J. L. Wallace, I. F. Gow and M. Warnock, The life and death of breast cancer cells: proposing a role for the effects of phytoestrogens on potassium channels, *J. Membr. Biol.*, 2011, **242**, 53–67.
15 A. Masi, A. Becchetti, R. Restano-Cassulini, S. Polvani, G. Hofmann, A. M. Buccoliero, M. Paglierani, B. Pollo, G. L. Taddei, P. Gallina, N. Di Lorenzo, S. Franceschetti, E. Wanke and A. Arcangeli, hERG1 channels are overexpressed in glioblastoma multiforme and modulate VEGF secretion in glioblastoma cell lines, *Br. J. Cancer*, 2005, **93**, 781–792.
16 S. He, M. T. Moutaoufik, S. Islam, A. Persad, A. Wu, K. A. Aly, H. Fonge, M. Babu and F. S. Cayabyab, HERG channel and cancer: A mechanistic review of carcinogenic processes and therapeutic potential, *Biochim. Biophys. Acta, Rev. Cancer*, 2020, **1873**, 188355.
17 I. Staudacher, J. Jehle, K. Staudacher, H. W. Pledl, D. Lemke, P. A. Schweizer, R. Becker, H. A. Katus and D. Thomas, HERG K^+ channel-dependent apoptosis and cell cycle arrest in human glioblastoma cells, *PLoS One*, 2014, **9**, e88164.
18 K. B. Pointer, P. A. Clark, K. W. Eliceiri, M. S. Salamat, G. A. Robertson and J. S. Kuo, Administration of Non-Torsadogenic human Ether-à-go-go-Related Gene Inhibitors Is Associated with Better Survival for High hERG-Expressing Glioblastoma Patients, *Clin. Cancer Res.*, 2017, **23**, 73–80.
19 S. Kalyaanamoorthy and K. H. Barakat, Development of Safe Drugs: The hERG Challenge, *Med. Res. Rev.*, 2018, **38**, 525–555.
20 M. Nasir-Moin, L. I. Wadiura, V. Sacalean, D. Juros, M. Movahed-Ezazi, E. K. Lock, A. Smith, M. Lee, H. Weiss, M. Müther, D. Alber, S. Ratna, C. Fang, E. Suero-Molina, S. Hellwig, W. Stummer, K. Rössler, J. A. Hainfellner, G. Widhalm, B. Kiesel, D. Reichert, M. Mischkulnig, R. Jain, J. Straehle, N. Neidert, O. Schnell, J. Beck, J. Trautman, S. Pastore, D. Pacione, D. Placantonakis, E. K. Oermann, J. G. Golfinos, T. C. Hollon, M. Snuderl, C. W. Freudiger, D. H. Heiland and D. A. Orringer,

Localization of protoporphyrin IX during glioma-resection surgery via paired stimulated Raman histology and fluorescence microscopy, *Nat. Biomed. Eng.*, 2024, **8**, 672–688.

21 K. Mizusawa, Y. Takaoka and I. Hamachi, Specific cell surface protein imaging by extended self-assembling fluorescent turn-on nanoprobes, *J. Am. Chem. Soc.*, 2012, **134**, 13386–13395.

22 K. Mizusawa, Y. Ishida, Y. Takaoka, M. Miyagawa, S. Tsukiji and I. Hamachi, Disassembly-driven turn-on fluorescent nanoprobes for selective protein detection, *J. Am. Chem. Soc.*, 2010, **132**, 7291–7293.

23 C. Attwooll, E. Lazzerini Denchi and K. Helin, The E2F family: specific functions and overlapping interests, *EMBO J.*, 2004, **23**, 4709–4716.

24 H. Chen, H. Liu and G. Qing, Targeting oncogenic Myc as a strategy for cancer treatment, *Signal Transduction Targeted Ther.*, 2018, **3**, 5.

25 H. Z. Chen, S. Y. Tsai and G. Leone, Emerging roles of E2Fs in cancer: an exit from cell cycle control, *Nat. Rev. Cancer*, 2009, **9**, 785–797.

26 I. C. Wang, Y. J. Chen, D. Hughes, V. Petrovic, M. L. Major, H. J. Park, Y. Tan, T. Ackerson and R. H. Costa, Forkhead box M1 regulates the transcriptional network of genes essential for mitotic progression and genes encoding the SCF (Skp2-Cks1) ubiquitin ligase, *Mol. Cell. Biol.*, 2005, **25**, 10875–10894.

27 M. Carmena, M. Wheelock, H. Funabiki and W. C. Earnshaw, The chromosomal passenger complex (CPC): from easy rider to the godfather of mitosis, *Nat. Rev. Mol. Cell Biol.*, 2012, **13**, 789–803.

28 G. L. Moldovan and A. D. D'Andrea, How the fanconi anemia pathway guards the genome, *Annu. Rev. Genet.*, 2009, **43**, 223–249.

29 P. González-Rodríguez, M. Cheray, J. Füllgrabe, M. Salli, P. Engskog-Vlachos, L. Keane, V. Cunha, A. Lupa, W. Li, Q. Ma, K. Dreij, M. G. Rosenfeld and B. Joseph, The DNA methyltransferase DNMT3A contributes to autophagy long-term memory, *Autophagy*, 2021, **17**, 1259–1277.

30 T. Maruyama and N. N. Noda, Autophagy-regulating protease Atg4: structure, function, regulation and inhibition, *J. Antibiot.*, 2017, **71**, 72–78.

31 X. Chen and J. R. Cubillos-Ruiz, Endoplasmic reticulum stress signals in the tumour and its microenvironment, *Nat. Rev. Cancer*, 2021, **21**, 71–88.

32 Y. Wang, X. Huang, J. Zhou, X. Yang, D. Li, H. Mao, H. H. Sun, N. Liu and J. Lian, Trafficking-deficient G572R-hERG and E637K-hERG activate stress and clearance pathways in endoplasmic reticulum, *PLoS One*, 2012, **7**, e29885.

33 A. T. Dennis, L. Wang, H. Wan, D. Nassal, I. Deschenes and E. Ficker, Molecular determinants of pentamidine-induced hERG trafficking inhibition, *Mol. Pharmacol.*, 2012, **81**, 198–209.

34 Y. Jiang, J. Zhang, F. Meng and Z. Zhong, Apolipoprotein E Peptide-Directed Chimeric Polymersomes Mediate an Ultrahigh-Efficiency Targeted Protein Therapy for Glioblastoma, *ACS Nano*, 2018, **12**, 11070–11079.

35 J. A. Swanson and D. F. Kern, Characterization of pulmonary endothelial charge barrier, *Am. J. Physiol.*, 1994, **266**, H1300–H1303.

36 X. Zhang, T. Liu, Q. Li, M. Li and L. Du, Aggregation-Induced Emission: Lighting Up hERG Potassium Channel, *Front. Chem.*, 2019, **7**, 54.

37 Z. Liu, Y. Zhou, L. Du and M. Li, Novel intramolecular photoinduced electron transfer-based probe for the Human Ether-a-go-go-Related Gene (hERG) potassium channel, *Analyst*, 2015, **140**, 8101–8108.

38 Z. Liu, B. Wang, Z. Ma, Y. Zhou, L. Du and M. Li, Fluorogenic probe for the human Ether-a-Go-Go-Related Gene potassium channel imaging, *Anal. Chem.*, 2015, **87**, 2550–2554.

39 Z. Liu, T. Jiang, B. Wang, B. Ke, Y. Zhou, L. Du and M. Li, Environment-Sensitive Fluorescent Probe for the Human Ether-a-go-go-Related Gene Potassium Channel, *Anal. Chem.*, 2016, **88**, 1511–1515.

40 Z. Qiao, Q. Zhou, H. Zhang, N. Wei, Y. Zhang and K. Wang, The visualization of hERG channels in living cells via a fluorescent probe regulated by the synergy between solvatochromism and molecular rotation based on simple targeting of the group 4-benzylaniline, *Chem. Commun.*, 2019, **55**, 5515–5518.